

Comparative analysis of dayside magnetic reconnection models in global magnetosphere simulations

C. M. Komar,¹ R. L. Fermo,¹ P. A. Cassak¹

Abstract.

We test and compare a number of existing models predicting the location of magnetic reconnection at Earth's dayside magnetopause for various solar wind conditions. We employ robust image processing techniques to determine the locations where each model predicts reconnection to occur. The predictions are then compared to the magnetic separators, the magnetic field lines separating different magnetic topologies. The predictions are tested in distinct high-resolution simulations with interplanetary magnetic field (IMF) clock angles ranging from 30 to 165 degrees in global magnetohydrodynamic simulations using the three-dimensional Block-Adaptive Tree Solarwind Roe-type Upwind Scheme (BATS-R-US) code with a uniform resistivity, although the described techniques can be generally applied to any self-consistent magnetosphere code. Additional simulations are carried out to test location model dependence on IMF strength and dipole tilt. We find that most of the models match large portions of the magnetic separators when the IMF has a southward component, with the models saying reconnection occurs where the local reconnection rate and reconnection outflow speed are maximized performing best. When the IMF has a northward component, none of the models tested faithfully map the entire magnetic separator, but the maximum magnetic shear model is the best at mapping the separator in the cusp region where reconnection has been observed. Predictions for some models with northward IMF orientations improve after accounting for plasma flow shear parallel to the reconnecting components of the magnetic fields. Implications for observations are discussed.

1. Introduction

Magnetic reconnection occurs in plasmas where oppositely directed magnetic fields merge, effectively break and transfer their magnetic energy into kinetic energy and heat. This process occurs between the interplanetary magnetic field (IMF) and the terrestrial magnetic field at the dayside magnetopause, transferring solar wind plasma into near-Earth space; this is the first step in the Dungey cycle of magnetospheric convection [Dungey, 1961]. However, predicting where magnetic reconnection occurs at Earth's dayside magnetopause for arbitrary solar wind conditions has been the subject of studies for nearly fifty years and remains a challenging problem. Knowledge of where reconnection occurs at Earth's magnetopause is crucial for developing a quantitative prediction of geomagnetic activity for space weather applications and to support satellite missions studying magnetic reconnection, such as NASA's upcoming Magnetospheric Multiscale (MMS) mission [Burch and Drake, 2009; Moore et al., 2013].

In the classical sketches of Dungey [1961, 1963], reconnection occurs at the subsolar point for due southward IMF and near the polar cusps for due northward IMF orientations (ignoring Earth's dipole tilt). However, much less is known about where reconnection occurs when the IMF makes an arbitrary clock angle θ_{IMF} with the Earth's dipole axis. The location of dayside magnetic reconnection was originally discussed in terms of anti-parallel [Crooker, 1979]

or component reconnection, either with a uniform out-of-plane (guide) magnetic field [Sonnerup, 1974; Gonzalez and Mozer, 1974] or equal and opposite components of the reconnecting magnetic field [Cowley, 1976]; the latter is known to not be valid. A number of literature reviews have been written on this subject [Dorelli et al., 2007; Paschmann, 2008; Fuselier et al., 2011; Guo et al., 2013]; the upshot is that both component and anti-parallel reconnection have been seen in observations and simulations. This implies that neither model can explain all the data so models going beyond them are necessary.

Some recent models suggest that reconnection occurs where some parameter is maximized which produces reconnection at an optimum efficiency. One such model is the maximum magnetic shear model [Trattner et al., 2007], an extension of the anti-parallel reconnection hypothesis. This model suggests that reconnection occurs where the magnetic shear angle between the magnetospheric and magnetosheath magnetic fields is a maximum. Three related models suggest reconnection occurs where the reconnection outflow speed is maximized [Swisdak and Drake, 2007], the reconnection rate is maximized (Shay, private communication, 2009; [Borovsky, 2013]), and the reconnecting field's magnetic energy is maximized [Hesse et al., 2013]. Other models suggest that reconnection occurs where the current density is a maximum [Alexeev et al., 1998] or where the magnetospheric magnetic field and the draped IMF are bisected [Moore et al., 2002].

There are a number of studies testing some of these models in different contexts. The maximum magnetic shear model was shown to be consistent with observations of magnetic reconnection at planetary magnetopauses with data from Cluster [Trattner et al., 2007; Dunlop et al., 2011], THEMIS [Trattner et al., 2012], and Cassini [Fuselier et al., 2014]. Also, observations [Teh and Sonnerup, 2008] and simulations [Schreier et al., 2010] suggest that the maximization

¹Department of Physics and Astronomy, West Virginia University, Morgantown, West Virginia, USA

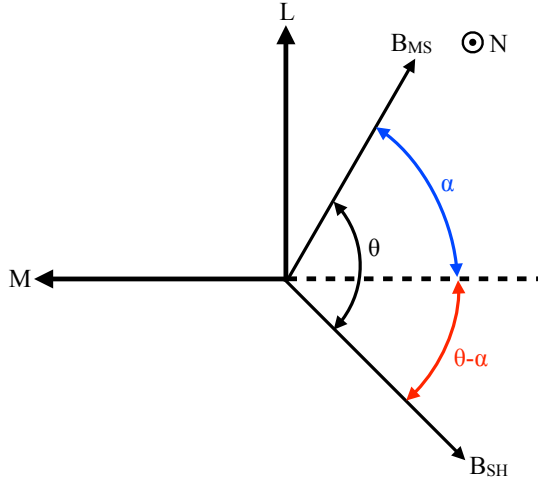


Figure 1. Schematic of an arbitrary magnetospheric magnetic field \mathbf{B}_{MS} making an angle θ with the magnetosheath magnetic field \mathbf{B}_{SH} in the boundary normal (LMN) coordinate system. The angle α is the angle the magnetospheric field makes with the M axis. Adapted from *Sonnerup* [1974] and *Swisdak and Drake* [2007].

of the asymmetric reconnection outflow speed controls the location and orientation of reconnection, although it is difficult to distinguish maximum outflow speed from maximum reconnection rate. The angle of bisection hypothesis has been tested with observations and in global magnetospheric simulations [*Pulkkinen et al.*, 2010] and in two-dimensional (2D) reconnection simulations [*Hesse et al.*, 2013].

One reason the location of reconnection at the dayside magnetopause is difficult to predict is that reconnection does not occur at a single point, but rather occurs along a line of finite extent. Magnetopause reconnection occurs along the line that separates magnetic fields of different topologies - solar wind and closed magnetospheric field lines merge and reconnect, resulting in open field lines. This line is called the magnetic separator [*Cowley*, 1973; *Stern*, 1973; *Siscoe*, 1987; *Lau and Finn*, 1990; *Siscoe et al.*, 2001; *Parnell et al.*, 2010], and is the three-dimensional (3D) analog of the 2D X-line. There is observational [*Xiao et al.*, 2007; *Pu et al.*, 2013; *Guo et al.*, 2013] and numerical [*Hu et al.*, 2004; *Laitinen et al.*, 2006, 2007; *Dorelli et al.*, 2007; *Dorelli and Bhatnagarjee*, 2008, 2009; *Hu et al.*, 2009; *Pulkkinen et al.*, 2010; *Ouellette et al.*, 2010; *Peng et al.*, 2010; *Cnossen et al.*, 2012; *Komar et al.*, 2013] evidence for the existence of separators throughout Earth's magnetosphere.

Consequently, a careful assessment of the correctness of the recent models for the location and orientation of reconnection begins with a comparison of their predictions to the measured magnetic separators. To do so, we interpret the models, as *Trattner et al.* [2007] has done with the maximum magnetic shear model, as predicting the collections of points that locally maximize a particular quantity rather than the single point that globally maximizes the quantity in question.

The goal of this study is to systematically test the recent models against the separators arising in self-consistent global simulations of the magnetosphere. To do so, we employ image processing techniques to unambiguously determine each model's prediction in our simulations. Each model's prediction is then compared with the magnetic separator determined with the algorithm described in *Komar et al.* [2013]; this algorithm has been shown to work for IMF with an arbitrary orientation. The present study tests each

model's agreement with the separators for various IMF clock angle θ_{IMF} , IMF strength B_{IMF} , and dipole tilt angle. We also present a test of one possible way to incorporate the effects of a flow shear parallel to the reconnecting fields into the models based on reconnection outflow speed and reconnection rate.

The layout of this paper is as follows: Section 2 reviews the models of dayside reconnection location that we test in the present study. Section 3 describes our methodology: the method used to determine the magnetopause, a robust image processing algorithm to determine each model's prediction, and details of our global magnetospheric simulations. Our results are presented in Section 4. A summary of our results and applications are discussed in Section 5.

2. Reconnection Location Models

This section reviews the models tested in this study. We employ the boundary normal (LMN) coordinate system. The N direction is the magnetopause normal corresponding to the inflow direction, the L direction corresponds to the reconnecting component of the magnetic field, and the M direction gives the direction of the out-of-plane (guide) magnetic field, completing the right-handed triplet. Figure 1, adapted from *Sonnerup* [1974] and *Swisdak and Drake* [2007], displays the magnetospheric and magnetosheath magnetic fields \mathbf{B}_{MS} and \mathbf{B}_{SH} at the magnetopause viewed along the inflow direction. These two fields point in arbitrary directions in the L - M plane, making a magnetic shear angle of θ with each other. The angle α is the angle \mathbf{B}_{MS} makes with the M axis and is constrained to occur within the range $0 < \alpha < \theta$. It is tacitly assumed that the magnetic field components along the N axis are weak.

In the maximum magnetic shear model [*Trattner et al.*, 2007], reconnection occurs at magnetopause locations where the magnetic shear angle θ between the magnetospheric and magnetosheath magnetic fields is a maximum. This model identifies the anti-parallel reconnection locations of *Crooker* [1979] with high fidelity, while also identifying additional locations away from the anti-parallel regions where θ is locally a maximum. The magnetic shear angle θ is calculated from the magnetospheric and magnetosheath magnetic fields as

$$\cos \theta = \frac{\mathbf{B}_{MS} \cdot \mathbf{B}_{SH}}{B_{MS} B_{SH}}. \quad (1)$$

Alternative explanations have suggested that reconnection occurs at locations where some measure of reconnection efficiency is maximized. In the model of *Swisdak and Drake* [2007], reconnection on the dayside is oriented (has an angle α) to maximize the reconnection outflow speed $c_{A,out}$. In a subsequent model, reconnection orients so as to maximize the reconnection electric field E (*Shay*, private communication, 2009), [*Borovsky*, 2013]). To calculate the predictions from these models at the dayside magnetopause, one needs the plasma parameters of the magnetosheath and magnetosphere, where asymmetries in the magnetic field and plasma density strongly affect reconnection. The scaling of asymmetric reconnection was developed for 2D antiparallel reconnection using conservation of mass and energy [*Cassak and Shay*, 2007] to obtain an expression for the asymmetric outflow speed

$$c_{A,out}^2 \sim \frac{B_{MS,L} B_{SH,L} (B_{MS,L} + B_{SH,L})}{\mu_0 (\rho_{MS} B_{SH,L} + \rho_{SH} B_{MS,L})} \quad (2)$$

and for the asymmetric electric field

$$E \sim c_{A,out} \frac{B_{MS,L} B_{SH,L}}{B_{MS,L} + B_{SH,L}} \frac{2\delta}{L}, \quad (3)$$

where ρ_{MS} and ρ_{SH} are the upstream magnetospheric and magnetosheath plasma mass densities, respectively, and δ and L are the half-width and half-length of the diffusion region. Equation (3) is valid independent of dissipation mechanism [Cassak and Shay, 2008, 2009]; the present study employs a resistivity η and the reconnection rate for asymmetric collisional, or Sweet-Parker, reconnection is [Cassak and Shay, 2007]

$$E_{SP} \sim \sqrt{\frac{\eta c_{A,out}}{\mu_0 L}} B_{MS,L} B_{SH,L}. \quad (4)$$

From Fig. 1, the reconnecting component of the upstream magnetospheric magnetic field can be written as

$$B_{MS,L} = B_{MS} \sin \alpha \quad (5)$$

and for the magnetosheath as

$$B_{SH,L} = B_{SH} \sin(\theta - \alpha). \quad (6)$$

The asymmetric outflow speed is maximized by setting

$$\frac{\partial c_{A,out}^2}{\partial \alpha} = 0$$

and solving for α [Swisdak and Drake, 2007]. A similar approach is used to maximize E (Shay, private communication, 2009; [Borovsky, 2013]). In practice, we interpret these as saying that the local $c_{A,out}$ and E can be found at every location on the magnetopause by finding α at every location, and that reconnection occurs where the parameter is a local maximum. We note in passing that this approach assumes that any nonzero B_M component of either magnetic field does not affect the outflow speed or reconnection rate. This is not likely to be correct in the real magnetosphere where finite Larmor radius effects are important, but should be accurate for the MHD simulations in the present study. Another limitation of the present formulation of these arguments is that they neglect the importance of the plasma bulk flow parallel to the reconnecting magnetic field components; we detail an attempt to account for this effect and measure the impact on the predictions of the asymmetric reconnection models in Section 4.4.

More recently, Hesse *et al.* [2013] suggested that the reconnection rate is proportional to the product of the reconnecting component's magnetic energies,

$$E \propto B_{MS,L}^2 B_{SH,L}^2, \quad (7)$$

and reconnection maximizes this product. Applying a maximization argument with respect to α gives a solution of $\alpha = \theta/2$; this is equivalent to previous arguments where the guide field bisects the merging magnetosheath and magnetospheric magnetic fields [Moore *et al.*, 2002; Borovsky, 2008].

We also test the model that predicts reconnection to occur where the current density magnitude $|\mathbf{J}|$ is a maximum [Alexeev *et al.*, 1998]. A related approach has been to look at the divergence of the Poynting vector. Reconnection has been located by measuring this quantity in observations [Anekallu *et al.*, 2013] and simulations [Papadopoulos *et al.*, 1999; Palmroth *et al.*, 2003; Laitinen *et al.*, 2006, 2007; Pulkkinen *et al.*, 2010; Palmroth *et al.*, 2012; Hoilijoki *et al.*, 2014]. In steady-state, the divergence of the Poynting vector is

$$\nabla \cdot \left(\frac{\mathbf{E} \times \mathbf{B}}{\mu_0} \right) \sim -\mathbf{E} \cdot \mathbf{J},$$

where \mathbf{E} is the electric field given by Ohm's law. The present study employs a large explicit resistivity, to be described in Section 3.4. In this system, the divergence of the Poynting

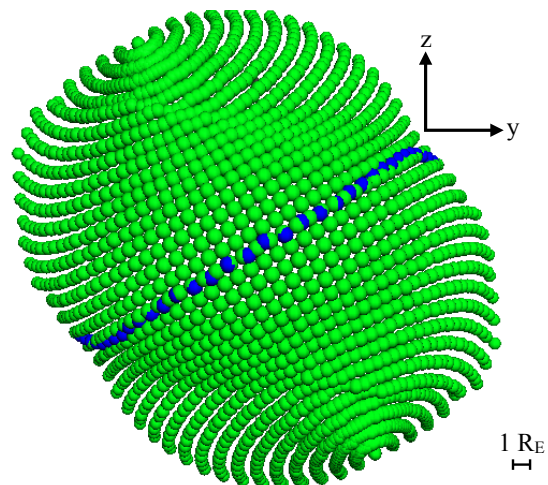


Figure 2. Magnetopause locations (green) from maxima in the current density's magnitude in a simulation with $\theta_{IMF} = 120^\circ$. The magnetic separator (blue) is shown for reference.

vector simplifies to $-\eta J^2$ at the reconnection site. We therefore argue that, up to a scaling factor, the Poynting vector's divergence would give similar results as the maximum current density magnitude argument for this study.

For completeness, we also test the component reconnection hypothesis as originally proposed by Sonnerup [1974] and Gonzalez and Mozer [1974], even though observations [Gosling *et al.*, 2007; Gosling, 2007; Teh and Sonnerup, 2008; Phan *et al.*, 2009, 2010; Gosling and Phan, 2013; DiBraccio *et al.*, 2013] and simulations [Schreier *et al.*, 2010] suggest the model is not valid. In this model, the local reconnection geometry orients itself such that the M component of the magnetic field is uniform, which, using the notation in Fig. 1, implies

$$\tan \alpha = \frac{b - \cos \theta}{\sin \theta}, \quad (8)$$

where $b = B_{MS}/B_{SH}$. This model places an additional constraint on the orientation angle α , with valid solutions only when the magnetic shear angle θ is greater than the critical shear angle $\theta_c = \cos^{-1}(1/b)$.

3. Methodology

Each of the models discussed in the previous section suggest reconnection at the dayside magnetopause occurs where some parameter is a local maximum. We model our approach after Trattner *et al.* [2007], who identified a curve corresponding to where the magnetic shear angle θ was a local maximum at the magnetopause. The magnetospheric magnetic field was modeled using the T96 model [Tsyganenko, 1995] and the Cooling model is used for the draped magnetosheath magnetic field [Cooling *et al.*, 2001] to calculate θ at many locations on the dayside magnetopause. The local shear angle θ was plotted as a function of the magnetopause's y and z coordinates (it was projected into the $x = 0$ plane) and maxima in this shear angle map were determined by finding maxima along cuts parallel to the IMF (K. Trattner, private communication, 2013).

The following sections detail how we robustly identify the magnetopause and calculate model predictions in our global magnetospheric simulations.

3.1. Identification of the Magnetopause and Plasma Parameter Sampling

To identify the magnetopause in our global magnetospheric simulations, we modify the method of *Němeček et al.* [2011]. (One may alternatively adopt the method described in *Palmroth et al.* [2003] to identify the magnetopause using streamlines, although this is not tested here.) The current density magnitude is sampled radially from $7 \leq r < 20$ Earth radii (R_E) at our highest grid cell resolution ($0.125 R_E$). The location of maximum current density at smallest r is identified as the magnetopause and this location's coordinates \mathbf{r}_{MP} are saved; the chosen sampling range excludes the ring current, but we take additional care by ensuring each point has a radial distance within $2 R_E$ of the previous point's radial distance. We employ spherical coordinates in the Geocentric Solar Magnetospheric (GSM) system, where the azimuthal angle ϕ is measured from the $+x$ axis and the polar angle θ is measured from the $+z$ axis; we discretize both into 5° increments. (Other increments were tested and found to converge to the 5° results.) We use an azimuthal range of $-130^\circ \leq \phi \leq 130^\circ$ to map the magnetopause for northward IMF orientations ($\theta_{IMF} = [30^\circ, 60^\circ, 90^\circ]$ for the purposes of this study) and $-110^\circ \leq \phi \leq 110^\circ$ for southward IMF orientations ($\theta_{IMF} = [120^\circ, 150^\circ, 165^\circ]$); the polar angle has a range $0^\circ \leq \theta \leq 180^\circ$ for both northward and southward IMF orientations.

An example of this process can be seen in Fig. 2, displaying the magnetopause surface as green spheres for a simulation with IMF clock angle 120° that will be described in Section 3.4. Additionally, the separator for this simulation from *Komar et al.* [2013] is plotted in blue. It lies within the magnetopause surface, as it should, confirming this method. The grid is rotated out of the ecliptic plane; the spherical coordinate system is rotated counter-clockwise about the $+x$ axis by an angle $\theta_{IMF}/2$. This is done to achieve near uniform sampling near the separator and each model's prediction, *i.e.* near $\theta \approx 90^\circ$ in the rotated frame.

Once the approximate location of the magnetopause has been determined, the local plasma parameters of the magnetosphere and magnetosheath are sampled. The appropriate way to do this is to sample along the magnetopause normal $\hat{\mathbf{n}}$ at each magnetopause position \mathbf{r}_{MP} . One may perform a minimum variance analysis (MVA) on the magnetic field [*Sonnerup and Cahill*, 1967] to determine the magnetopause normal. However, we find in practice this results in incorrect magnetopause normals since the magnetospheric and magnetosheath magnetic fields are parallel near the separator, violating the core assumption of MVA.

Instead, the normal is calculated with the method described in *Hoppe et al.* [1992]. The algorithm is to take a single point on the magnetopause \mathbf{r}_{MP} and find its four nearest neighbors \mathbf{r}_k on the magnetopause, with $k \in [1, 2, 3, 4]$. Calculate the difference vector $\mathbf{r}_k - \mathbf{r}_{MP}$, which gives the distance from the point on the magnetopause and its k th nearest neighbor. Then, construct the covariant matrix \mathbf{M} , whose ij element is

$$M_{ij}(\mathbf{r}_{MP}) = \sum_k (\mathbf{r}_k - \mathbf{r}_{MP})_i (\mathbf{r}_k - \mathbf{r}_{MP})_j, \quad (9)$$

where i and j refer to the x , y , or z component in GSM coordinates. The eigenvector corresponding to the minimum eigenvalue of \mathbf{M} is the magnetopause normal; this normal direction is chosen to point away from Earth, *i.e.*, $\hat{\mathbf{x}} \cdot \hat{\mathbf{n}} \geq 0$, and has been confirmed by inspection. This procedure has a physical interpretation of placing several planes at \mathbf{r}_{MP} with arbitrary orientations; the normal of the plane that minimizes the distance between the plane and the nearest neighbors is the magnetopause's normal.

The plasma parameters are sampled along the normal vector $\hat{\mathbf{n}}$ at our highest resolution ($0.125 R_E$) between $\mathbf{r}_{MP} - (5 R_E) \hat{\mathbf{n}}$ and $\mathbf{r}_{MP} + (5 R_E) \hat{\mathbf{n}}$. To accurately measure

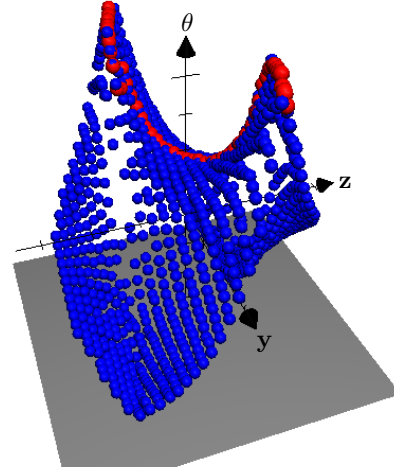


Figure 3. Magnetic shear angle θ (blue spheres) as a function of the magnetopause's y and z coordinates and the corresponding ridge of maximum magnetic shear angle (red spheres) in a simulation with $\theta_{IMF} = 120^\circ$.

the asymptotic plasma densities and magnetic fields undergoing magnetic reconnection, we employ the method used by *Cassak and Shay* [2009] for systems with asymmetries in either parameter. The current density is measured along $\hat{\mathbf{n}}$ to determine where it falls to $1/e$ of its maximum value in the magnetosheath. The distance between the current maximum and this location is the current sheet's half-thickness δ . The upstream plasma parameters of the magnetosphere are measured at $\mathbf{r}_{MP} - (2\delta) \hat{\mathbf{n}}$ and those of the magnetosheath at $\mathbf{r}_{MP} + (2\delta) \hat{\mathbf{n}}$. We confirm the measured magnetospheric and magnetosheath magnetic fields and densities are representative of the asymptotic values, as desired. The raw upstream magnetic fields can have a small normal component ($|B_n| \sim 1$ nT); these are removed prior to calculations. These values are used as \mathbf{B}_{MS} , \mathbf{B}_{SH} , ρ_{MS} , and ρ_{SH} for the models discussed in Section 2.

We note in passing that identifying the magnetopause as the maximum in the current density's magnitude has its limitations. One consequence of asymmetric reconnection systems is that the stagnation point separates from the reconnection X-line in 2D reconnection [*Cassak and Shay*, 2007]; the maximum of the out-of-plane current density also separates from the X-line. We will describe in Section 4.2 a test of reconnection location models in distinct simulations with IMF strengths of 20, 5, and 2 nT. The separation distances between the current density maximum and separator (the 3D version of the X-line) at the subsolar point in these simulations increase as the IMF strength is lowered, with distances of 0.07 (20 nT), 0.36 (5 nT), and 0.51 R_E (2 nT); the separation distances are resolved in the 5 and 2 nT simulations since our maximum resolution is $0.125 R_E$. In such systems, the current density maximum does not coincide with the magnetopause. For the purposes of this study, we assume this feature corresponds to a compression of the magnetopause in the $\hat{\mathbf{n}}$ direction at every point with minimal impact to each model's calculation as the sampling method described here measures the plasma parameters far enough away from the magnetopause location.

3.2. Finding Model Predictions Using Image Processing Techniques

Having found the approximate location of the magnetopause and the parameters locally governing reconnection

(ρ_{MS} , ρ_{SH} , \mathbf{B}_{MS} , \mathbf{B}_{SH}), the relevant quantities for each model are calculated at every point on the magnetopause. The magnetic shear angle θ is calculated from Eq. (1) at every point and is retained. Then at every point, α is discretized in the range $0 < \alpha < \theta$. For each value of α , $B_{MS,L}$ and $B_{SH,L}$ are calculated from Eqs. (5) and (6), and $c_{A,out}$, E_{SP} , and $B_{MS,L}^2 B_{SH,L}^2$ are calculated for that α . The α which maximizes the quantity in question is retained, and the value of $c_{A,out}$, E_{SP} , and $B_{MS,L}^2 B_{SH,L}^2$ is retained for that point. (One could also determine α from $\partial c_{A,out}/\partial\alpha = 0$ and $\partial E/\partial\alpha = 0$.) The current density magnitude is also retained at every point.

The results for each model are projected into the $x = 0$ plane, resulting in a 2D image $\mathcal{I}(y, z)$, where \mathcal{I} represents the quantity in question for each model. An example is shown in Fig. 3 for the maximum magnetic shear model, where \mathcal{I} corresponds to θ , which is plotted as the third dimension in blue spheres for the $\theta_{IMF} = 120^\circ$ simulation. The magnetic shear angle surface has a saddle shape, as do the surfaces for all the other models tested (not shown). This plot makes it clear that finding the collection of locations where the quantity in question is locally a maximum is tantamount to finding the ridge of local maxima in \mathcal{I} .

We achieve this in a robust way using image processing techniques using a ridge finding algorithm [Lindeberg, 1993, 1998]. First, we construct the Hessian tensor $H_{ij}(y, z) = \partial^2 \mathcal{I}(y, z) / \partial x_i \partial x_j$ via finite differencing at every point in the image. Diagonalizing the Hessian matrix defines a (p, q) coordinate system, where the eigenvector associated with the maximum absolute eigenvalue points in the direction of the local maxima. (Without loss of generality, we designate that eigenvector as $\hat{\mathbf{p}}$, the unit vector for the p direction.) Local maxima are determined by finding all locations where $\partial \mathcal{I} / \partial p = 0$ (local extrema test) and $\partial^2 \mathcal{I} / \partial p^2 < 0$ (local maxima test) using linear interpolation between nearest neighbors [Lindeberg, 1993].

The results of this technique for the maximum magnetic shear model for $\theta_{IMF} = 120^\circ$ are shown as the red spheres in Fig. 3. These red spheres clearly mark the ridge of the magnetic shear surface as desired. The methodology we employ yields qualitatively similar results to previous studies testing the maximum magnetic shear model for comparable magnetospheric and solar wind conditions (see Fig. 1 in *Fuselier et al.* [2011]), indicating this is an appropriate technique to determine each model's prediction. A more thorough comparison between these techniques will be presented in Section 4.1.

3.3. Determining Magnetic Separators

We employ the separator mapping algorithm of *Komar et al.* [2013] which has been shown to reliably trace the dayside portion of the magnetic separators connecting the magnetic nulls in global magnetosphere simulations for any IMF direction. When the IMF has a northward component, observations have shown that reconnection occurs poleward of the magnetic cusps (see *Wilder et al.* [2014], and references therein). We therefore trace portions of the magnetic separator nightward of the nulls in our simulations with $\theta_{IMF} = 30^\circ, 60^\circ, \text{ and } 90^\circ$.

In the separator tracing algorithm, a hemisphere is initially centered around a magnetic null. The hemisphere's surface, of radius $1 R_E$ for our purposes, is discretized into a grid. The magnetic field lines piercing the hemisphere at each grid point are traced to determine their magnetic topology: closed terrestrial, solar wind, and open either connected to the north or south magnetic poles. The approximate location of the separator is determined by finding where these four magnetic topologies meet on a hemisphere's surface. Then, another hemisphere is centered at the determined separator location, and the procedure is iterated to trace the separator. The dayside separator is traced from

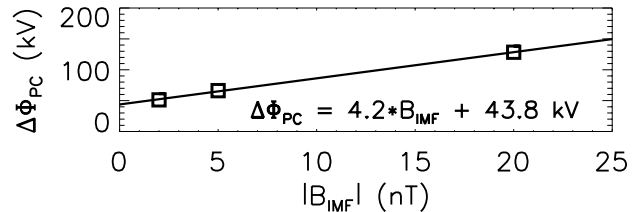


Figure 4. Cross polar cap potential difference $\Delta\Phi_{PC}$ in simulations with $|B_{IMF}| = 2, 5$ and 20 nT for $\theta_{IMF} = 120^\circ$. The potential difference is linear in $|B_{IMF}|$, so the polar cap is not saturated.

northern to southern null in this fashion and the nightside portion is traced back for $10 R_E$ from the magnetic nulls when the IMF has a northward orientation.

3.4. Magnetospheric Simulation Study

We perform global simulations using the Block Adaptive Tree Solarwind Roe-type Upwind Scheme (BATS-R-US) code [Powell et al., 1999; Gombosi et al., 2000; De Zeeuw et al., 2000; Tóth et al., 2012], although the methods detailed in the previous sections can be adapted to other global magnetospheric codes. Simulations are performed at NASA's Community Coordinated Modeling Center (CCMC) and are partially analyzed with CCMC's Kameleon software suite. The simulation domain is $-255 < x < 33$, $-48 < y < 48$, and $-48 < z < 48$, where distances are measured in R_E and the coordinate system is GSM.

The simulations are carried out using BATS-R-US version 8.01. The simulations are evolved for two hours (02:00:00) of magnetospheric time. We look at the 02:00:00 mark of simulation data as the system has achieved a quasi-steady state by this time. The standard high-resolution grid for CCMC simulations has 1,958,688 grid cells with a coarse resolution of $8 R_E$ in the far magnetotail, and a fine resolution of $0.25 R_E$ near the magnetopause. The present study employs a higher resolution grid of $0.125 R_E$ packed in the region $-15 < x, y, z < 15 R_E$, totaling 16,286,400 simulation grid cells.

The initial simulations do not employ a dipole tilt, although we include one later. All simulations use fixed solar wind inflow conditions. The solar wind has temperature $T = 232,100$ K, IMF strength 20 nT, number density $n = 20 \text{ cm}^{-3}$, and a solar wind velocity of $\mathbf{v} = -400 \text{ km/s } \hat{\mathbf{x}}$. We perform distinct simulations with IMF clock angles $\theta_{IMF} = 30^\circ, 60^\circ, 90^\circ, 120^\circ, 150^\circ, \text{ and } 165^\circ$. The IMF does not have a B_x component. Constant Pederson and Hall conductances of 5 mhos are used. The solar radio flux F10.7 index is set at a value of 150 .

The parameter regime of the solar wind in the present global magnetospheric simulations employed atypical IMF strengths and solar wind densities; both quantities are an order of magnitude higher than typically quiet solar wind conditions. This choice is made so the dayside magnetosphere is smaller, and the region of high resolution need not be as large. To ensure that the results are reliable, it is important to check that the polar cap is not saturated with these solar wind parameters [Lopez et al., 2010].

We measure the polar cap potential difference in three distinct simulations with $B_{IMF} = 2, 5, \text{ and } 20$ nT. These simulations have no dipole tilt, the IMF clock angle is fixed at 120° , and all other solar wind parameters are the same as before. Figure 4 displays the measured polar cap potential difference as a function of $|B_{IMF}|$. The plot clearly reveals that the potential difference remains linear as a function of IMF strength, implying the polar cap is not saturated. For comparison, *Lopez et al.* [2010], using LFM simulations, showed that the polar cap potential difference remains linear for $B_{IMF} < 11.25$ nT with solar wind density

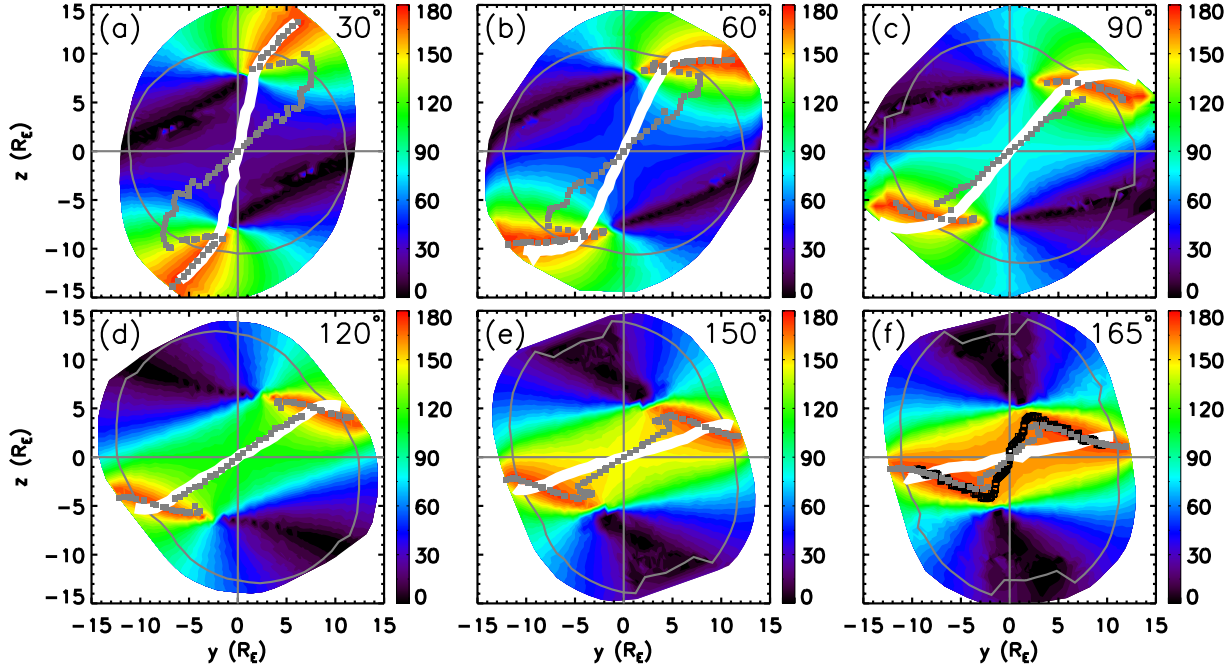


Figure 5. Results for the maximum magnetic shear model in simulations with θ_{IMF} of (a) 30° , (b) 60° , (c) 90° , (d) 120° , (e) 150° , and (f) 165° . The calculated magnetic shear angle θ is the color background, the gray squares display the curve of maximum magnetic shear angle, and the magnetic separator is displayed in white. The gray oval displays the magnetopause's projection in the $x = 0$ plane. Maxima determined from cuts along the IMF direction [Trattner *et al.*, 2007] are displayed as black squares in panel (f).

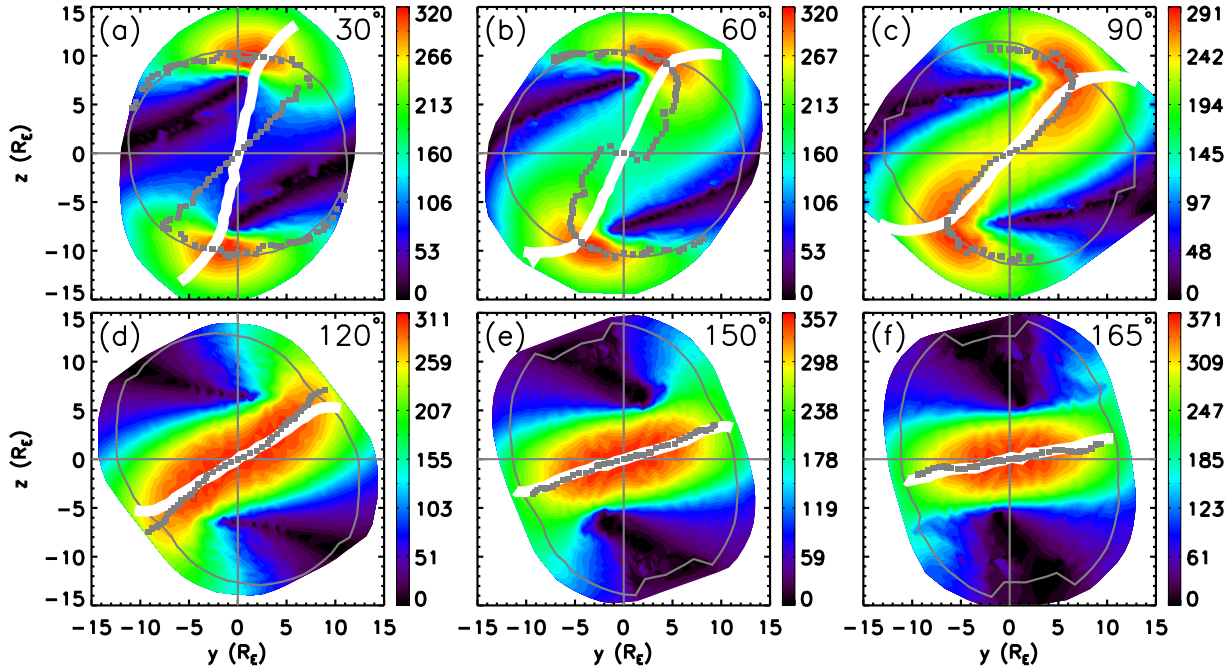


Figure 6. Results for the asymmetric outflow speed $c_{A,out}$. See the caption of Figure 5 for definitions.

$n_{\text{SW}} = 5 \text{ cm}^{-3}$ and for $B_{\text{IMF}} < 15 \text{ nT}$ when $n_{\text{SW}} = 8 \text{ cm}^{-3}$ using a solar wind speed of 400 km/s and ionospheric Pedersen conductance of 5 mhos . As our simulations employ $n_{\text{SW}} = 20 \text{ cm}^{-3}$, it is reasonable that we find the polar cap is not saturated for $B_{\text{IMF}} = 20 \text{ nT}$. Our measured viscous potential (the y -intercept) is 43.8 kV , consistent with the trend seen by Lopez *et al.* [2010], with their measured vis-

cous potentials of 33.9 and 41.9 kV for $n_{\text{SW}} = 5$ and 8 cm^{-3} , respectively. We are therefore confident that the polar cap is not saturated for our simulation parameters.

For the present simulations, we employ a uniform explicit resistivity η . It is known that Earth's magnetopause is collisionless, but including an explicit resistivity allows for reproducible results that are independent of the numerics. With the exception of the asymmetric Sweet-Parker recon-

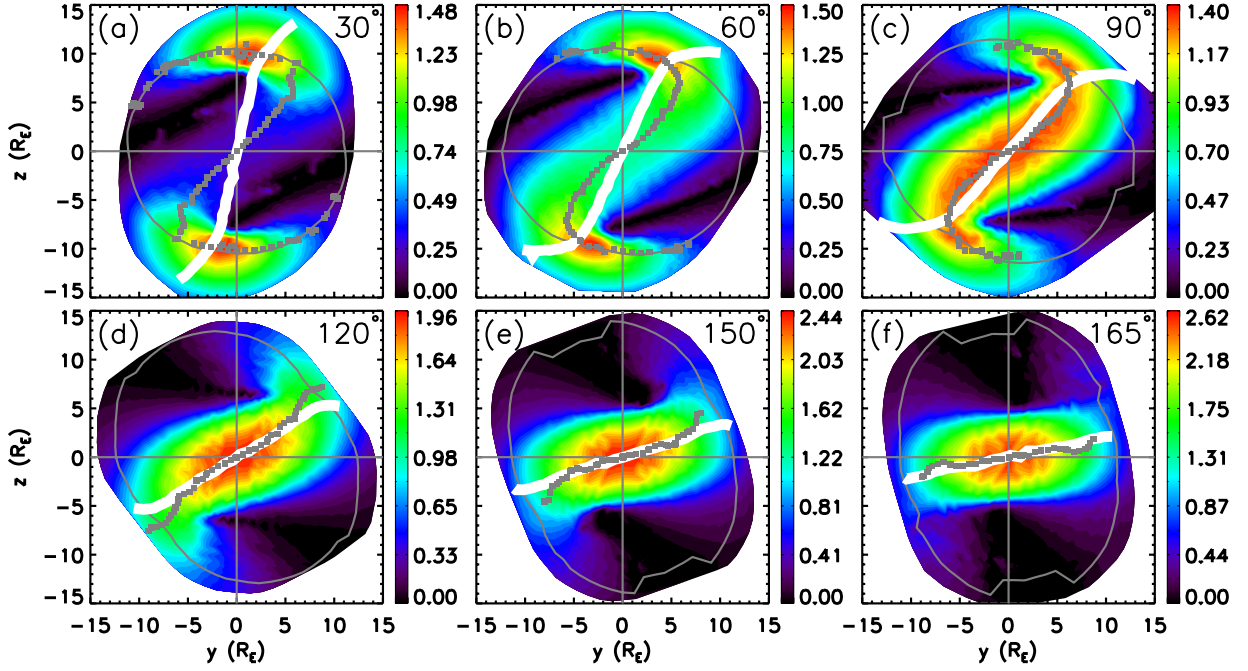


Figure 7. Results for the asymmetric Sweet-Parker reconnection rate E_{SP} . See the caption of Figure 5 for definitions.

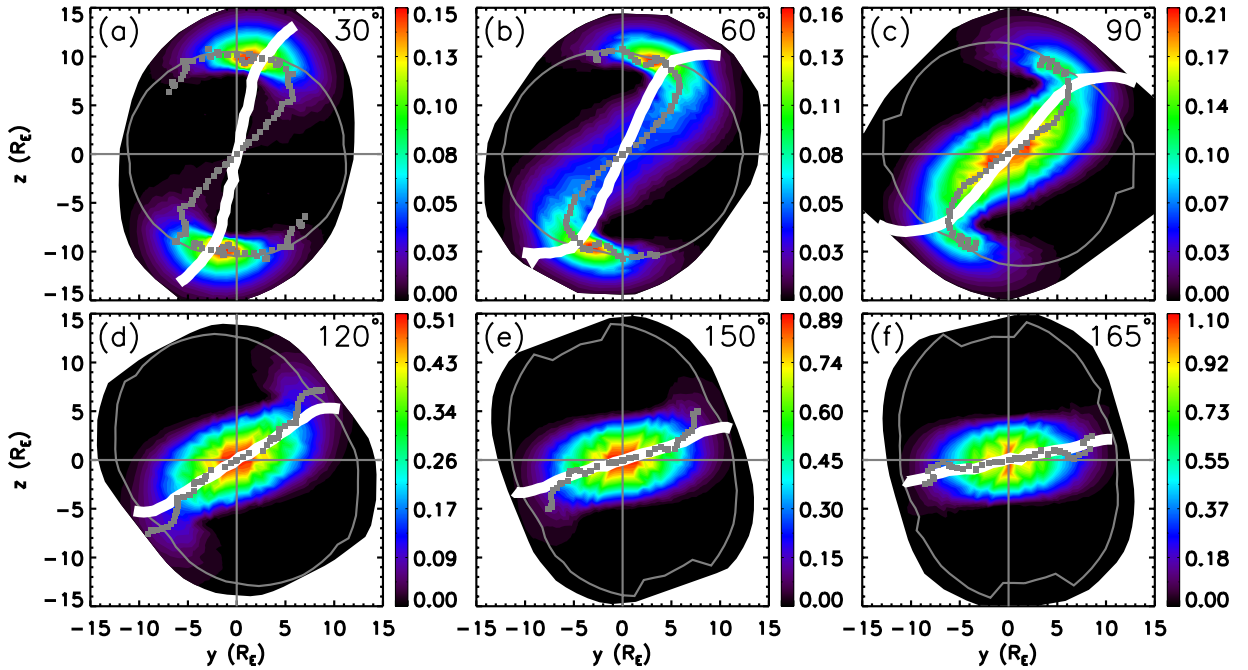


Figure 8. Results for the angle of bisection. See the caption of Figure 5 for definitions.

nection rate [Eq. (4)], all of the models selected for testing are independent of the reconnection dissipation mechanism. Therefore, the model predictions should likewise remain independent of this choice for *any* self-consistent magnetospheric model. We include an explicit resistivity $\eta/\mu_0 = 6.0 \times 10^{10} \text{ m}^2/\text{s}$ in our simulations, which allows us to sufficiently resolve the dayside magnetopause to determine the validity of the models tested. We refer the reader to Komar *et al.* [2013] for a more detailed discussion on the inclusion of an explicit resistivity.

3.5. Simulation Resolution

The numerical grid described in the present study is different from those of Komar *et al.* [2013] where the algorithm for finding separators was presented. The present simulations employed a resolution of $0.125 R_E$ in the region $-15 < x, y, z < 15 R_E$ whereas Komar *et al.* [2013] used a resolution of $0.125 R_E$ in the region $-6 < x < 10, -10 < y < 10, -5 < z < 5 R_E$, totaling a difference of ≈ 12.6 million simulation grid cells. The present study uses the larger high-resolution domain to ensure that the entire dayside magnetopause (and therefore the magnetic separators) is within the high-resolution domain. The magnetic

separators in the present simulations are not significantly different than those in *Komar et al.* [2013].

4. Results

We present results for the predicted locations for the models discussed in Section 2 and compare the results to magnetic separators. Figures 5-9 display the results in a common format. The quantity of interest is displayed as the background color, the model's prediction is displayed with solid gray squares, and the magnetic separators determined with the algorithm described in *Komar et al.* [2013] are displayed as the solid white line. The magnetopause's intersection with the $x = 0$ plane is displayed as the gray oval. The panels for each figure correspond to IMF clock angles θ_{IMF} of (a) 30° , (b) 60° , (c) 90° , (d) 120° , (e) 150° , and (f) 165° . Figure 5 displays the magnetic shear angle θ in degrees calculated from Eq. (1), Fig. 6 has the asymmetric outflow speed $c_{A,out}$ in km/s calculated from Eq. (2), Fig. 7 has the asymmetric Sweet-Parker reconnection rate E_{SP} in mV/m calculated from Eq. (4), Fig. 8 has the quantity $B_{\text{MS,L}}^2 B_{\text{SH,L}}^2$ from Eq. (7) in 10^8 nT^4 , and Figure 9 has the current density magnitude $|\mathbf{J}|$ in nA/m^2 .

Figure 10 displays the results for the uniform B_M component model. Plots (a) through (f) are for the same IMF clock angle simulations as previously discussed, with a few notable differences. The local B_M component (guide field) is calculated by determining the orientation angle α from Eq. (8), and rotating about the determined boundary normal $\hat{\mathbf{n}}$. The gray arrows in Fig. 10 display the projection of the magnetic field's M component in the $x = 0$ plane; locations without any vector displayed are where reconnection is predicted to be geometrically impossible. The magnetic separator is displayed as the solid black line, with the magnetopause's location in the $x = 0$ plane plotted in gray as before.

Section 4.1 discusses how the predictions of each model change with IMF clock angle for fixed solar wind conditions. We test the dependence on IMF strength of various models in Section 4.2. Section 4.3 describes results from two distinct simulations that include a dipole tilt with IMF clock angles 120° and 30° . Lastly, Section 4.4 discusses an attempt to incorporate the effects of a plasma flow shear on reconnection into the outflow speed and reconnection rate models from Section 2.

4.1. Clock Angle Dependence

Before assessing each model, we perform a more careful comparison between our ridge finding technique and the one in *Trattner et al.* [2007]. We plot the result using the technique of *Trattner et al.* [2007], which finds maxima of magnetic shear angle along cuts parallel to the IMF direction, as black squares in Fig. 5(f) for the $\theta_{\text{IMF}} = 165^\circ$ simulation. While qualitatively similar, there are apparent differences. If one takes cuts along different directions (not shown), the detected locations change, and can move to locations on the other side of the image processing ridge. This underscores two points: (1) it is important to employ a user-independent technique, such as image processing, to locate each model's prediction as the *Trattner et al.* [2007] algorithm exhibits sensitivity to the cut orientation and (2) the noticeable changes in the prediction are caused by the relative flatness in the saddle region that occurs near the subsolar point in these results. Consequently, there are uncertainties that could cause minor changes to the predictions which should be kept in mind in the interpretation of these results.

We now focus on the predictions of each model and how they compare with the separators for all IMF clock angles. Of the models tested, the maximum magnetic shear as shown has the largest discrepancy with the dayside portion of the magnetic separators in simulations without a

dipole tilt, but could have better agreement in light of the uncertainties discussed above. More importantly, only the maximum magnetic shear model reproduces the portion of the magnetic separator nightward of the magnetic nulls with high fidelity. These portions of the magnetic separators coincide with the antiparallel regions and are near the magnetic cusps, consistent with early expectations [*Dungey*, 1961, 1963; *Crooker*, 1979] and with observations (see *Wilder et al.* [2014], and references therein).

The asymmetric reconnection arguments ($c_{A,out}$ and E_{SP}) show better agreement with the magnetic separators overall for the simulations with southward IMF orientations. The ridges of these models rotate around the x axis, as does the separator, although there are differences between the separators and the model predictions for clock angles $\theta_{\text{IMF}} \leq 120^\circ$.

The predictions for the angle of bisection and the maximum current density models have a similar shape as the other models' predictions through the subsolar point. Figures 8(a)-(c) and 9(a)-(c) show intersections between the model predictions and magnetic separators near the antiparallel regions and at the subsolar point for $\theta_{\text{IMF}} \leq 90^\circ$. The predictions of these arguments do follow the separator more closely for southward IMF orientations, and do not rotate around the magnetopause for northward orientations.

The uniform B_M component model would accurately predict the separator if the arrows point along the separator. They clearly do not; at the subsolar point, the measured orientation angle α relative to the magnetospheric magnetic field is (see Fig. 1): (a) N/A (reconnection is geometrically impossible), (b) 46.9° , (c) 53.1° , (d) 64.1° , (e) 76.8° , and (f) 83.6° . These angles are inconsistent with the orientation angles α_{Sep} of the magnetic separators (a) 10.3° , (b) 21.7° , (c) 35.8° , (d) 55.3° , (e) 71.2° , and (f) 77.5° . The discrepancies between the magnetic field's M component and the orientation of the magnetic separators provide further evidence that this description does not accurately predict the orientation of magnetic reconnection, consistent with previous observations [*Teh and Sonnerup*, 2008] and simulations [*Schreier et al.*, 2010].

4.2. IMF Strength Dependence

Equations (2) and (4) have strong dependencies on the magnetospheric and magnetosheath magnetic field strengths. The magnetospheric magnetic field strength is usually much larger than that of the magnetosheath, and does not vary much for the chosen simulation parameters. This implies that the reconnection efficiency models depend strongly on the magnetosheath magnetic field strength B_{SH} . Meanwhile, the maximum magnetic shear model is expected to be independent of B_{SH} . We therefore vary B_{SH} to see if it helps to distinguish among these models.

We lower the IMF strength from 20 nT to 5 and 2 nT in separate simulations and use $\theta_{\text{IMF}} = 120^\circ$ with all other simulation parameters unchanged. Figure 11 displays the results from these simulations. The top row displays the magnetic shear angle in degrees, the middle row has the asymmetric outflow speed in km/s, and the bottom row has the asymmetric Sweet-Parker reconnection rate in mV/m. Figures 11(a), (d), and (g) are for the $B_{\text{IMF}} = 20 \text{ nT}$ simulation, (b), (e), and (h) have $B_{\text{IMF}} = 5 \text{ nT}$, and (c), (f), and (i) use $B_{\text{IMF}} = 2 \text{ nT}$. As before, each model's prediction is plotted as the gray squares, the magnetic separators are displayed in white.

We note in passing that the magnetopause is elongated along the IMF direction in the 20 nT plots of Fig. 11. This effect is consistent with observations [*Lavraud et al.*, 2013]

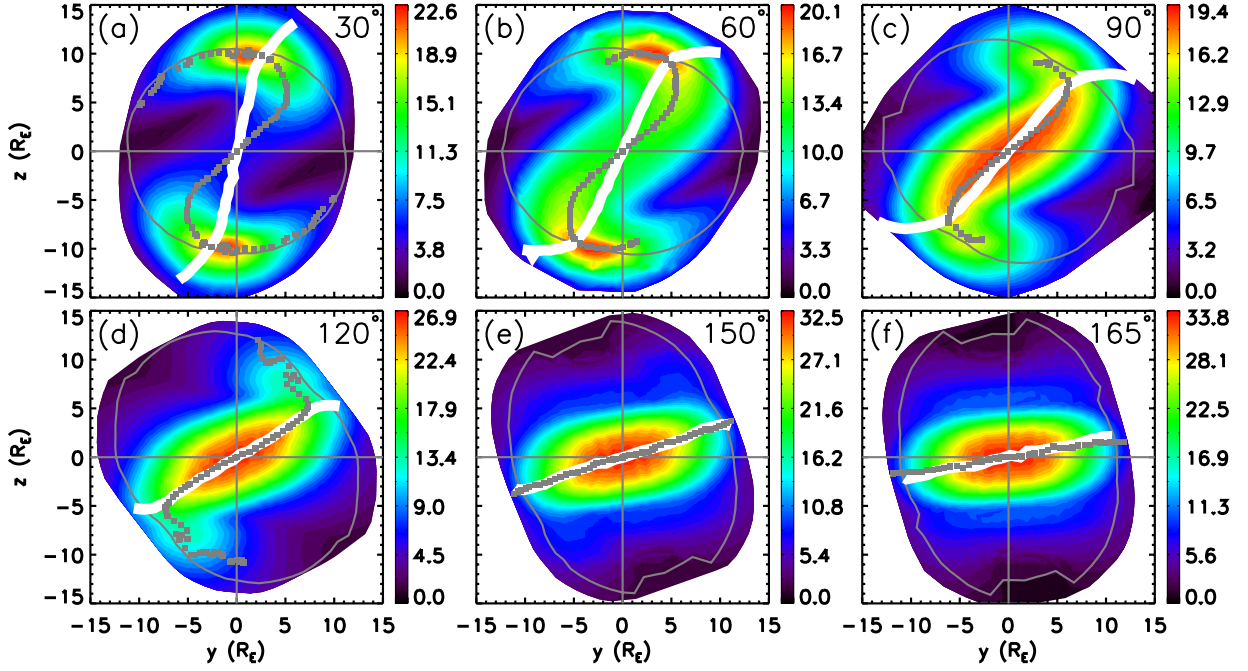


Figure 9. Results for the current density magnitude $|\mathbf{J}|$. See the caption of Figure 5 for definitions.

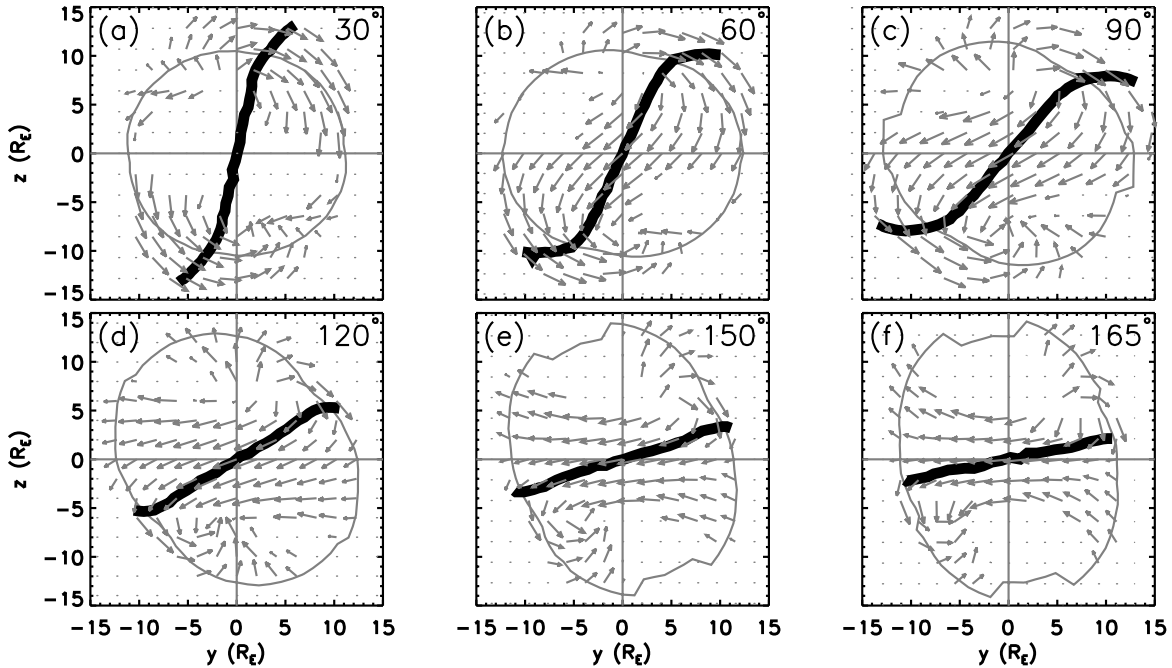


Figure 10. Results for the uniform B_M component model. Panels (a) through (f) are from the same simulations as in Figures 5-9. The y and z components of B_M are plotted as gray arrows and the magnetic separator is displayed in black.

and simulations [Lavraud and Borovsky, 2008] for low solar wind Alfvén Mach number.

The subsolar region in each simulation becomes increasingly asymmetric as the IMF strength is lowered; the measured magnetic field ratios are $b = B_{MS}/B_{SH} = 1.4, 4.1,$ and 11 for $B_{IMF} = 20, 5,$ and 2 nT, respectively. As seen in Fig. 11, each model's prediction becomes noisier for smaller B_{SH} due to the limitation of determining the magnetopause via the current maximum, as described in section 3.1.

Figures 11(a)-(c) show the maximum magnetic shear model remains relatively independent of the IMF strength as expected; this model's predictions have very similar structures as seen previously for arbitrary θ_{IMF} , making similar angles with the magnetospheric magnetic field of $49.6^\circ, 50.2^\circ,$ and 53.2° in simulations with $B_{IMF} = 20, 5,$ and 2 nT, respectively. This model maps large portions of the magnetic separator across the dayside magnetopause, consistent with previous results.

It is difficult to see differences between the asymmetric outflow speed and asymmetric Sweet-Parker reconnection

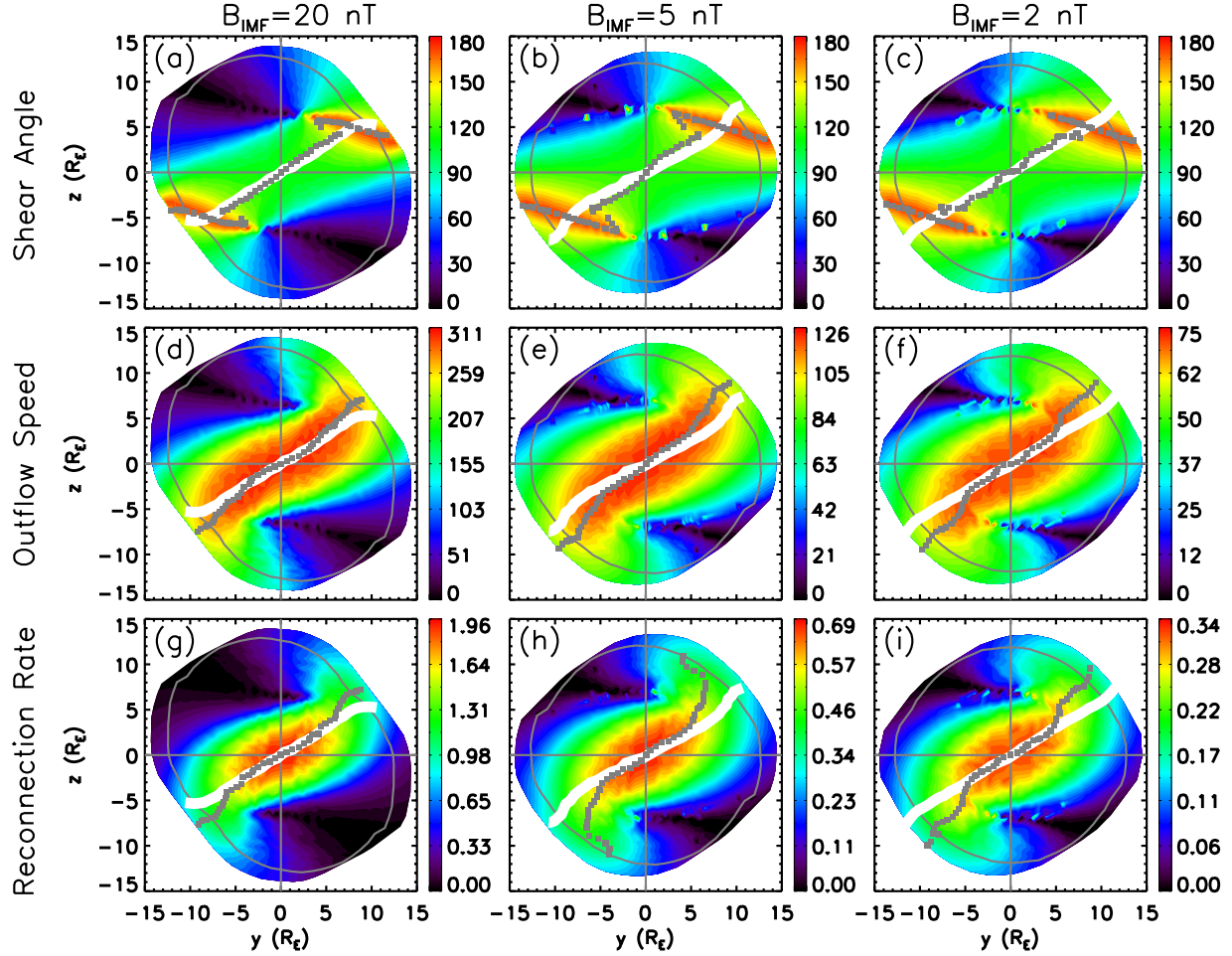


Figure 11. Results for testing model dependence on IMF strength for: (top row) the magnetic shear angle, (middle row) asymmetric outflow speed, and (bottom row) the asymmetric Sweet-Parker reconnection rate. Plots (a), (d) and (g) are for $B_{IMF} = 20$ nT, (b), (e), (h) are for $B_{IMF} = 5$ nT, and (c), (f), (i) for $B_{IMF} = 2$ nT. See the caption of Figure 5 for definitions.

rate models in Fig. 11. The predictions of both models closely map the magnetic separator in these simulations. For a more quantitative comparison between these models, we calculate each model's predicted orientation angle and compare these values to the separator's orientation at the subsolar point. The separator's orientation angle α_{Sep} measured from the magnetospheric magnetic field is 55.3° , 61.5° , and 56.2° in the $B_{IMF} = 20$, 5, and 2 nT simulations, respectively. The orientation of the ridges passing through the subsolar region for the asymmetric outflow speed make an angle α_V and, likewise, the asymmetric Sweet-Parker reconnection rate α_E are again measured from the magnetospheric magnetic field, with values $\alpha_V = 47.0^\circ$ and $\alpha_E = 51.0^\circ$ in the $B_{IMF} = 20$ nT simulation, $\alpha_V = 45.7^\circ$ and $\alpha_E = 49.7^\circ$ for $B_{IMF} = 5$ nT, and finally, $\alpha_V = 47.4^\circ$ and $\alpha_E = 47.4^\circ$ with $B_{IMF} = 2$ nT.

The orientation angle α_E decreases as IMF strength is lowered, while α_V displays a minimum when $B_{IMF} = 5$ nT. However, α_{Sep} is maximum when $B_{IMF} = 5$ nT. All of the models tested have predictions that are reasonably close, but none show perfect agreement with the orientation at the subsolar point. This implies that these models will need further modification to accurately predict the orientation of reconnection at Earth's subsolar magnetopause.

4.3. Dipole Tilt Dependence

Including a dipole tilt can alter the location of magnetic reconnection. For example, *Trattner et al.* [2007] showed that the prediction of the maximum magnetic shear angle moves southward under positive dipole tilt (as measured from the $+z$ axis in the $x-z$ GSM plane, *i.e.* the northern magnetic pole pointing Sunward), and likewise moves northward for negative dipole tilt when paired with southward IMF orientations. Reconnection in simulations with a dipole tilt [*Park et al.*, 2006; *Palmroth et al.*, 2012; *Cnossen et al.*, 2012; *Hoilijoki et al.*, 2014].

Employing a more realistic dipole model of Earth may assist in distinguishing among the models. Note in Figs. 5-9 the model predictions intersect the magnetic separators at the subsolar point and near the anti-parallel region for all IMF clock angles. These intersections result from symmetry; including a dipole tilt will break this symmetry making it easier to distinguish which model predicts the magnetic separator.

We present the results of two additional simulations that employ a $+15^\circ$ dipole tilt. The same solar wind parameters described in Section 3.4 are used in separate simulations with IMF clock angles of 120° (Fig. 12) and 30° (Fig. 13). Figures 12 and 13 display each model's prediction as the grey squares, where the maximized quantity is: (a) the magnetic shear angle θ in degrees, (b) the asymmetric outflow speed $c_{A,out}$ in km/s, (c) the asymmetric Sweet-Parker reconnection rate E_{SP} in mV/m, (d) the quantity $B_{MS,L}^2 B_{SH,L}^2$ from

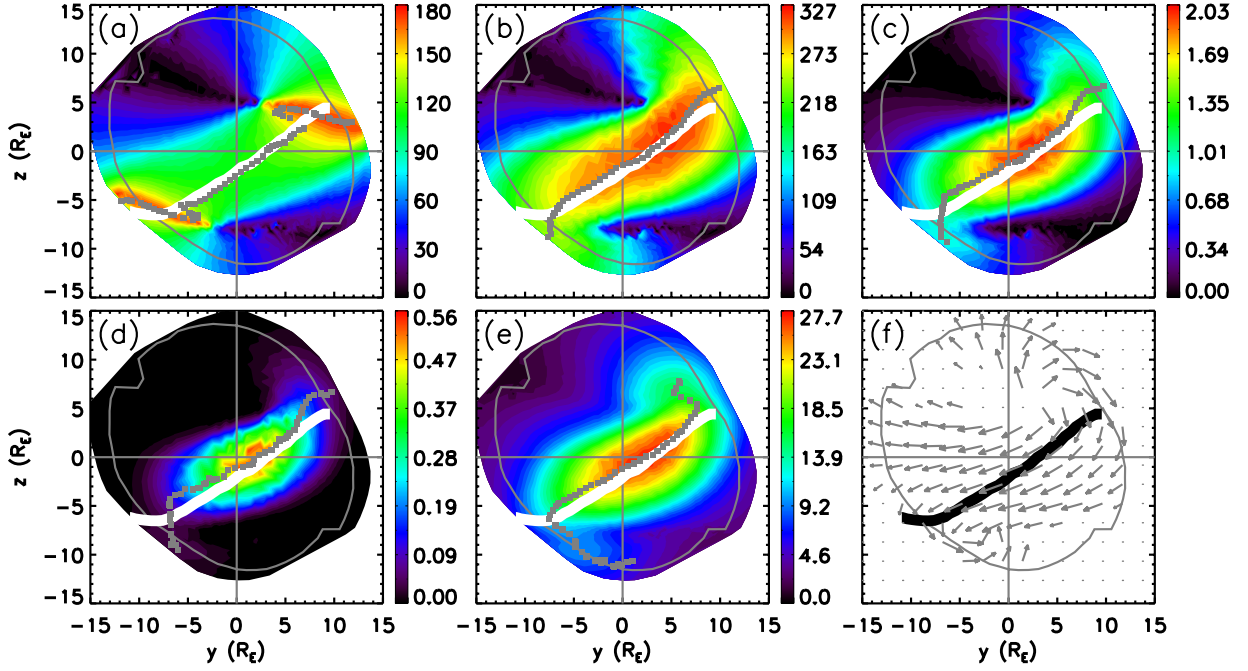


Figure 12. Results from a simulation with a dipole tilt of $+15^\circ$ and a southward IMF orientation with clock angle 120° : (a) the magnetic shear angle θ , (b) the asymmetric outflow speed $c_{A,out}$, (c) the asymmetric Sweet-Parker reconnection rate E_{SP} , (d) the angle of bisection, (e) the current density magnitude $|\mathbf{J}|$, and (e) the y and z components of the uniform B_M component. See the caption of Figure 5 for definitions.

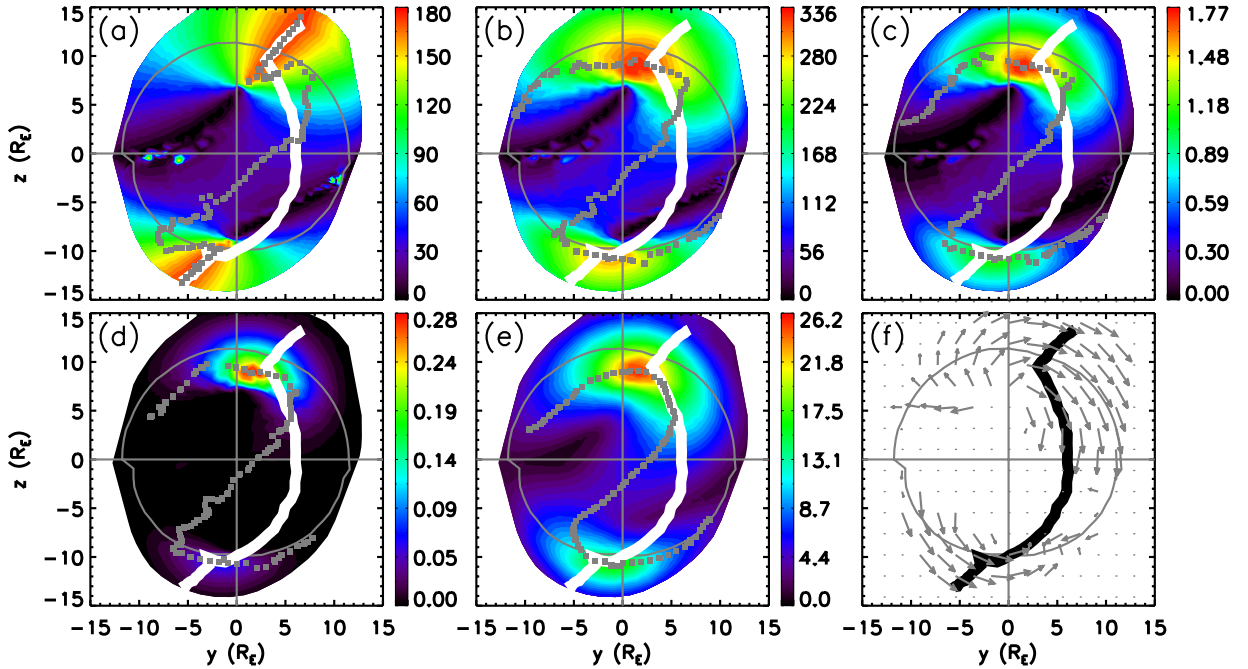


Figure 13. Results from a simulation with dipole tilt of $+15^\circ$ and a northward IMF orientation with clock angle 30° . See the caption of Figure 12 for definitions.

Eq. (7) in 10^8 nT^4 , and (e) the current density magnitude $|\mathbf{J}|$ in nA/m^2 , and (f) the projection of the uniform B_M component in the $x = 0$ plane. The magnetic separators are displayed in white for (a)-(e) and black in (f) as before.

In Fig. 12, each model appears to map the magnetic separator reasonably well with a southward IMF orientation and

positive dipole tilt. The maximum magnetic shear model's prediction follows the separator more closely than any other model when the dipole tilt is present. The other models map the separator more closely in the northern, dusk quadrant in Figs. 12(b)-(e) than any other quadrant. [We use down ($-y$), dusk ($+y$), southern ($-z$), northern ($+z$) to indicate position in the y - z GSM plane.] Figure 12(f) shows that

the uniform B_M component model again fails to map the magnetic separator in any quadrant.

The results for IMF clock angle 30° and positive dipole tilt in Fig. 13 are significantly different. The separator moves approximately 45° in longitude duskward of the $+x_{\text{GSM}}$ axis. The model predictions intersect the magnetic separator in the northern, dusk and southern, dawn quadrants, with the maximum current density mapping the largest portion of the separator in the northern, dusk quadrant. The maximum magnetic shear model is again the only model that faithfully reproduces the nightward portion of the magnetic separator. Most importantly, no model maps any part of the separator in the southern, dusk quadrant.

4.4. Effect of a Flow Shear

Existing models have thus far ignored the impact of solar wind flow around the magnetopause. The tailward flow of magnetosheath plasma around the magnetopause can have a component parallel to the reconnecting component of the magnetic field, which is known to impact the efficiency of reconnection [Chen and Morrison, 1990; La Belle-Hamer et al., 1994, 1995; Cassak and Otto, 2011]. This effect potentially could alter models based on reconnection efficiency.

The incorporation of a plasma flow shear into equations (2) and (4) is ongoing work. Based on preliminary work (C. E. Doss et al., private communication, 2014), we hypothesize that the predictions for the outflow speed [Cassak, 2011] and reconnection rate [Cassak and Otto, 2011] for symmetric reconnection with a flow shear can be generalized for asymmetric reconnection by replacing the symmetric outflow speed c_A with the asymmetric outflow speed $c_{A,out}$ from Eq. (2), giving

$$c_{\text{Shearflow}} = c_{A,out} \sqrt{1 - \frac{v_s^2}{c_{A,out}^2}}, \quad (10)$$

and

$$E_{\text{Shearflow}} = E_{SP} \left(1 - \frac{v_s^2}{c_{A,out}^2} \right), \quad (11)$$

where E_{SP} is given by Eq. (4). The flow shear speed v_s is given by

$$v_s = \frac{v_{\text{SH,L}} - v_{\text{MS,L}}}{2}$$

and $v_{\text{SH,L}}$ and $v_{\text{MS,L}}$ are the magnetosheath and magnetopause flow in the L direction, respectively.

We test to see if these expressions alter the predictions of the reconnection efficiency arguments. As before, α is discretized to calculate the asymmetric arguments $c_{A,out}$ and E_{SP} while the L direction is rotated around the magnetopause normal for each α . The velocities on each side of the magnetopause are measured 3δ upstream along $\hat{\mathbf{n}}$ and $v_{\text{SH,L}}$ and $v_{\text{MS,L}}$ are calculated by taking the L -component for each α . We calculate the modified reconnection outflow speed and electric field using equations (10) and (11) as a function of α . (For $v_s > c_{A,out}$, $c_{\text{Shearflow}}$ and $E_{\text{Shearflow}}$ are set to zero as reconnection should not be possible.) Modified model predictions are determined with image processing techniques as described in Section 3.2.

Figure 14 displays results for two different clock angles: the top row are from the simulation with $\theta_{\text{IMF}} = 30^\circ$ and the bottom row has $\theta_{\text{IMF}} = 120^\circ$. Panels (a) and (e) are results without corrections for flow shear and are replicated from Fig. 6. Likewise, panels (c) and (g) are from Fig. 7 for the reconnection rate. Panels (b) and (f) give results that incorporate a flow shear in the calculation of the outflow speed and (d) and (h) on the reconnection rate. The model predictions more closely map the separator when the IMF has a northward orientation after accounting for the flow

shear, and remain largely unchanged with a southward IMF orientation. Quantifying this effect in the northward IMF simulation, the prediction for $c_{A,out}$ makes an angle α of 44.7° with the magnetospheric magnetic field, and changes to 32.7° after accounting for the flow shear; the separator makes an angle of $\alpha_{SEP} = 10.3^\circ$. Likewise, the prediction of E_{SP} makes an angle of 43.2° and is 29.7° after including a flow shear. Changes to the orientation angles for each model's prediction in the southward IMF simulation are much smaller changing from 47.0° to 46.4° for the outflow speed, and change from 51.0° to 52.1° for the reconnection electric field; the separator has $\alpha_{SEP} = 55.3^\circ$ for this simulation. A further test of this model was performed for the 30° clock angle with positive dipole tilt simulation. The results (not shown) revealed improvement of the model predictions in some areas, and worse agreement in others, but still differed significantly from the separator.

The relative importance of a flow shear is understood as a result of general flow patterns around the magnetopause. For southward IMF, reconnection occurs near the ecliptic plane where the magnetosheath flow and magnetospheric convection are tangential to this plane. Thus, any flow shear parallel to the magnetic field is small and reconnection should not be strongly affected. However, the magnetosheath flow at high latitudes is quite large. When the IMF is northward, there is appreciable flow parallel to the reconnecting magnetic fields and may lead to the suppression of reconnection. The present results suggest that including flow shear improves the agreement between separators and model predictions for the reconnection efficiency arguments.

We note that the analysis here assumes that any v_M flow tangential to the L -components of the magnetic fields has no effect on the reconnection. This is unlikely to be the case, but including this is beyond the scope of the present study.

5. Conclusions

In this paper, we calculate the predictions of several magnetic reconnection location models at the dayside magnetopause in global resistive MHD simulations. Models tested are: the maximum magnetic shear model [Trattner et al., 2007], maximization of the asymmetric reconnection outflow speed [Swisdak and Drake, 2007], maximization of the asymmetric reconnection rate (Shay, private communication, 2009; [Borovsky, 2013]), the angle of bisection [Moore et al., 2002; Borovsky, 2008; Hesse et al., 2013], the maximization of the current density magnitude [Alexeev et al., 1998], and component reconnection (uniform B_M component) [Sonnerup, 1974; Gonzalez and Mozer, 1974]. The first five models predict reconnection to occur at locations where a given parameter is maximized. We employ robust image processing techniques to determine each model's prediction. Each model is tested in separate global magnetospheric simulations with various IMF orientations, IMF strengths, and with a dipole tilt. The predictions for each model are then compared to the magnetic separators to determine which model, if any, accurately predicts the location of reconnection at the dayside magnetopause. We summarize our findings:

1. For the chosen simulation parameters, we find that all models are within a few Earth radii (R_E) of the magnetic separators when the IMF has a southward orientation and no dipole tilt.

2. None of the models chosen for this study faithfully reproduce the entire magnetic separators when the IMF has a northward orientation and no dipole tilt. However, only the maximum magnetic shear model faithfully reproduces the portion of the separator nightward of the magnetic nulls where reconnection is expected to occur.

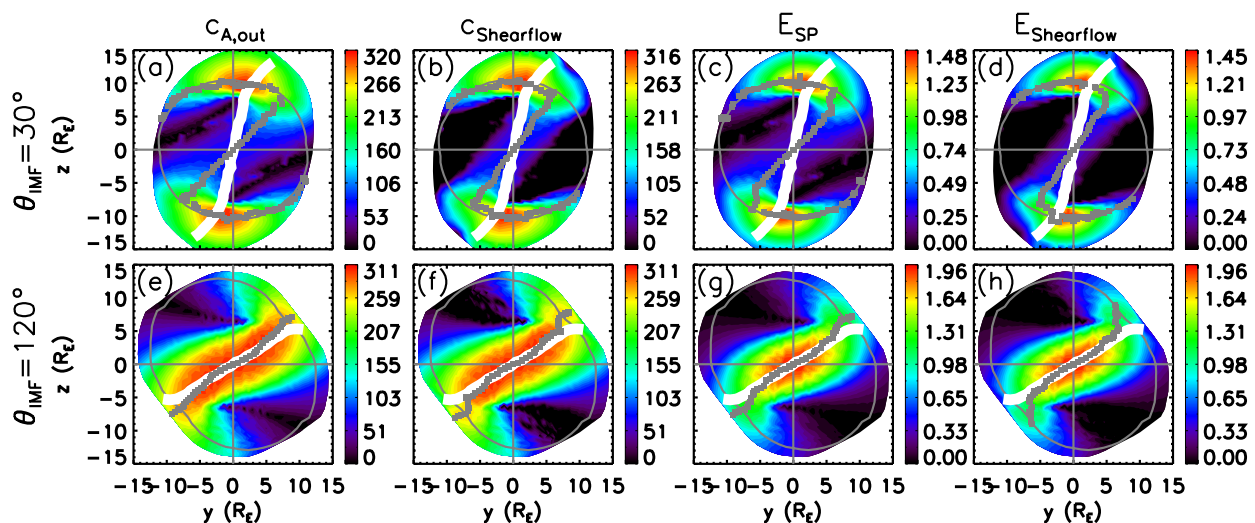


Figure 14. Results for testing the effects of flow shear on model predictions with (top row) $\theta_{\text{IMF}} = 30^\circ$ and (bottom row) 120° . Plots (a) and (e) are for the unmodified asymmetric outflow speed $c_{A,\text{out}}$, (b) and (f) are for the modified outflow speed $c_{\text{Shearflow}}$, (c) and (g) are for the unmodified asymmetric Sweet-Parker reconnection rate E_{SP} , and (d) and (h) are for the modified reconnection rate $E_{\text{Shearflow}}$. See the caption of Figure 5 for definitions.

3. The asymmetric outflow speed and asymmetric Sweet-Parker reconnection rate more closely map the magnetic separators than other models tested under southward IMF orientations and no dipole tilt. The maximum magnetic shear model has a fixed orientation at the subsolar magnetopause and does not rotate with the magnetic separators for different IMF clock angles in simulations without a dipole tilt.

4. As the IMF strength is varied with fixed clock angle, the magnetic separators display different orientations than the predictions of the magnetic shear angle, and the asymmetric outflow speed and Sweet-Parker reconnection rate models.

5. In simulations with a dipole tilt of $+15^\circ$, we find most of the models map the magnetic separators when the IMF clock angle is 120° . However, none of the models chosen for this study faithfully reproduce the entire magnetic separator for a northward IMF orientation of 30° . Again, only the maximum magnetic shear model traces the portion of the separator nightward of the magnetic nulls. The dayside portion of the magnetic separator in this simulation moves duskward by approximately 45° in longitude, as measured from the $+x_{\text{GSM}}$ axis.

6. Accounting for flow shear parallel to the reconnecting components of the magnetosheath and magnetospheric magnetic fields improve the performance of the asymmetric outflow speed and asymmetric reconnection rate models under northward IMF orientations. Predictions for southward IMF orientations are mostly unaffected.

In short, most of the models tested give results fairly close to the location of dayside reconnection for southward IMF orientations, but none are perfect. We conclude that the existing models may be good enough for a ball park estimate, but it remains unclear what physically controls the location of magnetic reconnection at the dayside magnetopause.

The present study employed a few underlying assumptions. We employed a uniform, explicit resistivity in our global MHD simulations even though Earth's magnetopause is collisionless; this choice ensures our simulations are well resolved, while reducing the likelihood of Flux Transfer Events (FTEs) [Russell and Elphic, 1978] in our simulations. However, recent advances have been made to trace magnetic separators in simulation when FTEs are present (A. Gloer et al., manuscript in preparation, 2014).

Most of the reconnection location models discussed here are independent of dissipation mechanism, so the present

results on the validity of each model should be independent of our choice to include an explicit resistivity. However, it is still unknown if the magnetic separators depend on dissipation mechanism. Future work will need to extend the present study to global Hall-MHD, hybrid, or kinetic simulations.

The analysis presented here has largely focused on the global process of magnetic reconnection by identifying the magnetic separators across the dayside magnetopause. At present, there is debate as to whether magnetic reconnection is a global or local phenomenon at the dayside magnetopause. We determined a model's prediction by maximizing a parameter related to reconnection at the dayside magnetopause. Our underlying assumption is that a particular model determines reconnection if that model faithfully reproduces the entire magnetic separator. Future work will need to assess this assumption by characterizing the locations on the magnetic separator where magnetic reconnection occurs.

Finally, the present study uses a small set of solar wind and magnetospheric conditions. The present work has ignored the effect of including an IMF B_x component. Previous studies found that under southward IMF orientations, the reconnection site moves northward for $B_x > 0$ and southward when $B_x < 0$ [Peng et al., 2010; Hoilijoki et al., 2014]. Additionally, we perform our analysis after the simulations have achieved steady-state, which does not capture the magnetosphere's response to dynamic solar wind conditions [Laitinen et al., 2006, 2007]. Understanding the response of Earth's magnetosphere for a broader range of solar wind conditions is of the utmost importance for realistic space weather forecasting, and will be the subject of future work.

Acknowledgments.

Support from NSF grant AGS-0953463 (CMK and PAC), NASA grant NNX10AN08A (PAC), and NASA West Virginia Space Grant Consortium (CMK) are gratefully acknowledged. We wish to acknowledge support from the International Space Science Institute in Bern, Switzerland. Simulations were performed at the Community Coordinated Modeling Center at Goddard Space Flight Center through their public Runs on Request system (<http://ccmc.gsfc.nasa.gov>). The CCMC is a multi-agency partnership between NASA, AFMC, AFOSR, AFRL, AFWA, NOAA, NSF and ONR. The BATS-R-US Model was developed

by the Center for Space Environment Modeling at the University of Michigan. The analysis presented here was made possible via the Kameleon and Space Weather Explorer software packages provided by the Community Coordinated Modeling Center at NASA Goddard Space Flight Center (<http://ccmc.gsfc.nasa.gov>). Software Developers are: M. M. Maddox, D. H. Berrios, and L. Rastaetter. The data used to produce the results of this paper are publicly available for free from CCMC. The authors would like to thank C. E. Doss, S. A. Fuselier, G. Paschmann, S. M. Petriner, D. G. Sibeck, V. M. Souza, and K. J. Trattner for their insight and interesting discussions.

References

- Alexeev, I. I., D. G. Sibeck, and S. Y. Bobrovnikov (1998), Concerning the location of magnetopause merging as a function of the magnetopause current strength, *J. Geophys. Res.*, *103*(A4), 6675–6684.
- Anekallu, C. R., M. Palmroth, H. E. J. Koskinen, E. Lucek, and I. Dandouras (2013), Spatial variation of energy conversion at the Earth’s magnetopause: Statistics from Cluster observations, *J. Geophys. Res.*, *118*(5), 1948–1959.
- Borovsky, J. E. (2008), The rudiments of a theory of solar wind/magnetosphere coupling derived from first principles, *J. Geophys. Res.*, *113*, A08228.
- Borovsky, J. E. (2013), Physical improvements to the solar wind reconnection control function for the Earth’s magnetosphere, *J. Geophys. Res.*, *118*(5), 2113–2121.
- Burch, J. L., and J. F. Drake (2009), Reconnecting magnetic fields, *Am. Sci.*, *97*, 392.
- Cassak, P. A. (2011), Theory and simulations of the scaling of magnetic reconnection with symmetric shear flow, *Phys. Plasmas*, *18*(7), 072106.
- Cassak, P. A., and A. Otto (2011), Scaling of the magnetic reconnection rate with symmetric shear flow, *Phys. Plasmas*, *18*(7), 074501.
- Cassak, P. A., and M. A. Shay (2007), Scaling of asymmetric magnetic reconnection: General theory and collisional simulations, *Phys. Plasmas*, *14*, 102114.
- Cassak, P. A., and M. A. Shay (2008), Scaling of asymmetric Hall reconnection, *Geophys. Res. Lett.*, *35*, L19102.
- Cassak, P. A., and M. A. Shay (2009), Structure of the dissipation region in fluid simulations of asymmetric magnetic reconnection, *Phys. Plasmas*, *16*, 055704.
- Chen, X. L., and P. J. Morrison (1990), Resistive tearing instability with equilibrium shear flow, *Phys. Fluids B*, *2*(3), 495–507.
- Cnossen, I., M. Wiltberger, and J. E. Ouellette (2012), The effects of seasonal and diurnal variations in the Earth’s magnetic dipole orientation on solar wind–magnetosphere–ionosphere coupling, *J. Geophys. Res.*, *117*(A11), A11211.
- Cooling, B. M. A., C. J. Owen, and S. J. Schwartz (2001), Role of the magnetosheath flow in determining the motion of open flux tubes, *J. Geophys. Res.*, *106*(A9), 18,763–18,775.
- Cowley, S. W. H. (1973), A qualitative study of the reconnection between the Earth’s magnetic field and an interplanetary field of arbitrary orientation, *Radio Sci.*, *8*(11), 903–913.
- Cowley, S. W. H. (1976), Comments on the merging of nonantiparallel magnetic fields, *J. Geophys. Res.*, *81*(19), 3455–3458.
- Crooker, N. U. (1979), Dayside merging and cusp geometry, *J. Geophys. Res.*, *84*(A3), 951–959.
- De Zeeuw, D., T. Gombosi, C. Groth, K. Powell, and Q. Stout (2000), An adaptive MHD method for global space weather simulations, *IEEE T. Plasma Sci.*, *28*, 1956.
- DiBraccio, G. A., J. A. Slavin, S. A. Boardsen, B. J. Anderson, H. Korth, T. H. Zurbuchen, J. M. Raines, D. N. Baker, R. L. McNutt, and S. C. Solomon (2013), MESSENGER observations of magnetopause structure and dynamics at Mercury, *J. Geophys. Res.*, *118*(3), 997–1008.
- Dorelli, J. C., and A. Bhattacharjee (2008), Defining and identifying three-dimensional magnetic reconnection in resistive magnetohydrodynamic simulations of Earth’s magnetosphere, *Phys. Plasmas*, *15*, 056504.
- Dorelli, J. C., and A. Bhattacharjee (2009), On the generation and topology of flux transfer events, *J. Geophys. Res.*, *114*, A06213.
- Dorelli, J. C., A. Bhattacharjee, and J. Raeder (2007), Separator reconnection at Earth’s dayside magnetopause under generic northward interplanetary magnetic field conditions, *J. Geophys. Res.*, *112*, A02202.
- Dungey, J. W. (1961), Interplanetary magnetic field and the auroral zones, *Phys. Rev. Lett.*, *6*, 47.
- Dungey, J. W. (1963), The structure of the exosphere, or adventures in velocity space, in *Geophysics: The Earth’s Environment*, edited by C. De Witt, J. Hieblot, and A. Lebeau, p. 505, Gordon Breach, New York.
- Dunlop, M. W., Q.-H. Zhang, Y. V. Bogdanova, K. J. Trattner, Z. Pu, H. Hasegawa, J. Berchem, M. G. G. T. Taylor, M. Volwerk, J. P. Eastwood, B. Lavraud, C. Shen, J.-K. Shi, J. Wang, D. Constantinescu, A. N. Fazakerley, H. Frey, D. Sibeck, P. Escoubet, J. A. Wild, Z. X. Liu, and C. Carr (2011), Magnetopause reconnection across wide local time, *Ann. Geophys.*, *29*(9), 1683–1697.
- Fuselier, S. A., K. J. Trattner, and S. M. Petriner (2011), Antiparallel and component reconnection at the dayside magnetopause, *J. Geophys. Res.*, *116*(A10), A10227.
- Fuselier, S. A., R. Frahm, W. S. Lewis, A. Masters, J. Mukherjee, S. M. Petriner, and I. J. Sillanpaa (2014), The location of magnetic reconnection at Saturn’s magnetopause: A comparison with Earth, *J. Geophys. Res.*, *116*(A10), A10227.
- Gombosi, T., D. DeZeeuw, C. Groth, and K. Powell (2000), Magnetospheric configuration for Parker-spiral IMF conditions: Results of a 3D AMR MHD simulation, *Adv. Space Res.*, *26*, 139.
- Gonzalez, W. D., and F. S. Mozer (1974), A quantitative model for the potential resulting from reconnection with an arbitrary interplanetary magnetic field, *J. Geophys. Res.*, *79*(28), 4186–4194.
- Gosling, J. T. (2007), Observations of magnetic reconnection in the turbulent high-speed solar wind, *Astrophys. J. Lett.*, *671*(1), L73.
- Gosling, J. T., and T. D. Phan (2013), Magnetic reconnection in the solar wind at current sheets associated with extremely small field shear angles, *Ap. J. Lett.*, *763*(2), L39.
- Gosling, J. T., T. D. Phan, R. P. Lin, and A. Szabo (2007), Prevalence of magnetic reconnection at small field shear angles in the solar wind, *Geophys. Res. Lett.*, *34*(15), L15110.
- Guo, R., Z. Pu, C. Xiao, X. Wang, S. Fu, L. Xie, Q. Zong, J. He, Z. Yao, J. Zhong, and J. Li (2013), Separator reconnection with antiparallel/component features observed in magnetotail plasmas, *J. Geophys. Res.*, pp. 6116–6126.
- Hesse, M., N. Aunai, S. Zenitani, M. Kuznetsova, and J. Birn (2013), Aspects of collisionless magnetic reconnection in asymmetric systems, *Phys. Plasmas*, *20*(6), 061210.
- Holljoki, S., V. M. Souza, B. M. Walsh, P. Janhunen, and M. Palmroth (2014), Magnetopause reconnection and energy conversion as influenced by the dipole tilt and the IMF B_x , *J. Geophys. Res.*, *119*(6), 4484–4494.
- Hoppe, H., T. DeRose, T. Duchamp, J. McDonald, and W. Stuetzle (1992), Surface reconstruction from unorganized points, *SIGGRAPH Comput. Graph.*, *26*(2), 71–78.
- Hu, S., A. Bhattacharjee, J. Dorelli, and J. M. Greene (2004), The spherical tearing mode, *Geophys. Res. Lett.*, *31*(19), L19806.
- Hu, Y. Q., Z. Peng, C. Wang, and J. R. Kan (2009), Magnetic merging line and reconnection voltage versus IMF clock angle: Results from global MHD simulations, *J. Geophys. Res.*, *114*, A08220.
- Komar, C. M., P. A. Cassak, J. C. Dorelli, A. Glocer, and M. M. Kuznetsova (2013), Tracing magnetic separators and their dependence on IMF clock angle in global magnetospheric simulations, *J. Geophys. Res.*, *118*(8), 4998–5007.
- La Belle-Hamer, A. L., A. Otto, and L. C. Lee (1994), Magnetic reconnection in the presence of sheared plasma flow: Intermediate shock formation, *Phys. Plasmas*, *1*(3), 706–713.
- La Belle-Hamer, A. L., A. Otto, and L. C. Lee (1995), Magnetic reconnection in the presence of sheared flow and density asymmetry: Applications to the Earth’s magnetopause, *J. Geophys. Res.*, *100*(A7), 11,875–11,889.
- Laitinen, T. V., P. Janhunen, T. I. Pulkkinen, M. Palmroth, and H. E. J. Koskinen (2006), On the characterization of magnetic reconnection in global MHD simulations, *Ann. Geophys.*, *24*, 3059.

- Laitinen, T. V., M. Palmroth, T. I. Pulkkinen, P. Janhunen, and H. E. J. Koskinen (2007), Continuous reconnection line and pressure-dependent energy conversion on the magnetopause in a global MHD model, *J. Geophys. Res.*, *112*, A11201.
- Lau, Y.-T., and J. M. Finn (1990), Three-dimensional kinematic reconnection in the presence of field nulls and closed field lines, *Astrophys. J.*, *350*, 672.
- Lavraud, B., and J. E. Borovsky (2008), Altered solar wind-magnetosphere interaction at low Mach numbers: Coronal mass ejections, *J. Geophys. Res.*, *113*(A9), A00B08.
- Lavraud, B., E. Larroque, E. Budnik, V. Génot, J. E. Borovsky, M. W. Dunlop, C. Foullon, H. Hasegawa, C. Jacquey, K. Nykyri, A. Ruffenach, M. G. T. Taylor, I. Dandouras, and H. Rème (2013), Asymmetry of magnetosheath flows and magnetopause shape during low Alfvén Mach number solar wind, *J. Geophys. Res.*, *118*(3), 1089–1100.
- Lindeberg, T. (1993), Discrete derivative approximations with scale-space properties: A basis for low-level feature extraction, *J. Math. Imaging and Vis.*, *3*(4), 349–376.
- Lindeberg, T. (1998), Edge detection and ridge detection with automatic scale selection, *Int. J. Comp. Vis.*, *30*(2), 117–156.
- Lopez, R. E., R. Bruntz, E. J. Mitchell, M. Wiltberger, J. G. Lyon, and V. G. Merkin (2010), Role of magnetosheath force balance in regulating the dayside reconnection potential, *J. Geophys. Res.*, *115*(A12), A12216.
- Moore, T., J. Burch, W. Daughton, S. Fuselier, H. Hasegawa, S. Petrinc, and Z. Pu (2013), Multiscale studies of the three-dimensional dayside X-line, *J. Atmos. Sol. Terr. Phys.*, *99*(0), 32–40.
- Moore, T. E., M.-C. Fok, and M. O. Chandler (2002), The dayside reconnection X line, *J. Geophys. Res.*, *107*(A10), 1332.
- Němeček, Z., J. Šafránková, A. Koval, J. Merka, and L. Přech (2011), MHD analysis of propagation of an interplanetary shock across magnetospheric boundaries, *J. Atmos. Sol. Terr. Phys.*, *73*(1), 20–29.
- Ouellette, J. E., B. N. Rogers, M. Wiltberger, and J. G. Lyon (2010), Magnetic reconnection at the dayside magnetopause in global Lyon-Fedder-Mobarry simulations, *J. Geophys. Res.*, *115*, A08222.
- Palmroth, M., T. I. Pulkkinen, P. Janhunen, and C.-C. Wu (2003), Stormtime energy transfer in global MHD simulation, *J. Geophys. Res.*, *108*(A1), 1048.
- Palmroth, M., R. C. Fear, and I. Honkonen (2012), Magnetopause energy transfer dependence on the interplanetary magnetic field and the Earth’s magnetic dipole axis orientation, *Ann. Geophys.*, *30*(3), 515–526.
- Papadopoulos, K., C. Goodrich, M. Wiltberger, R. Lopez, and J. Lyon (1999), The physics of substorms as revealed by the ISTP, *Phys. Chem. Earth C*, *24*(1–3), 189–202.
- Park, K. S., T. Ogino, and R. J. Walker (2006), On the importance of antiparallel reconnection when the dipole tilt and IMF B_y are nonzero, *J. Geophys. Res.*, *111*(A5), A05202.
- Parnell, C. E., A. L. Haynes, and K. Galsgaard (2010), Structure of magnetic separators and separator reconnection, *J. Geophys. Res.*, *115*(A2), A02102.
- Paschmann, G. (2008), Recent in-situ observations of magnetic reconnection in near-Earth space, *Geophys. Res. Lett.*, *35*(19), L19109.
- Peng, Z., C. Wang, and Y. Q. Hu (2010), Role of IMF B_x in the solar wind-magnetosphere-ionosphere coupling, *J. Geophys. Res.*, *115*, A08224.
- Phan, T. D., J. T. Gosling, and M. S. Davis (2009), Prevalence of extended reconnection X-lines in the solar wind at 1 AU, *Geophys. Res. Lett.*, *36*(9), L09108.
- Phan, T. D., J. T. Gosling, G. Paschmann, C. Pasma, J. F. Drake, M. Øieroset, D. Larson, R. P. Lin, and M. S. Davis (2010), The dependence of magnetic reconnection on plasma β and magnetic shear: Evidence from solar wind observations, *Astrophys. J. Lett.*, *719*(2), L199.
- Powell, K. G., P. L. Roe, T. J. Linde, T. I. Gombosi, and D. L. D. Zeeuw (1999), A solution-adaptive upwind scheme for ideal magnetohydrodynamics, *J. Comp. Phys.*, *154*, 284.
- Pu, Z. Y., J. Raeder, J. Zhong, Y. V. Bogdanova, M. Dunlop, C. J. Xiao, X. G. Wang, and A. Fazakerley (2013), Magnetic topologies of an in vivo FTE observed by Double Star/TC-1 at Earth’s magnetopause, *Geophys. Res. Lett.*, *40*(14), 3502–3506.
- Pulkkinen, T. I., M. Palmroth, H. E. J. Koskinen, T. V. Laitinen, C. C. Goodrich, V. G. Merkin, and J. G. Lyon (2010), Magnetospheric modes and solar wind energy coupling efficiency, *J. Geophys. Res.*, *115*(A3), A03207.
- Russell, C. T., and R. C. Elphic (1978), Initial ISEE magnetometer results: magnetopause observations, *Space Sci. Rev.*, *22*, 681.
- Schreier, R., M. Swisdak, J. F. Drake, and P. A. Cassak (2010), Three-dimensional simulations of the orientation and structure of reconnection X-lines, *Phys. Plasmas*, *17*(11), 110704.
- Siscoe, G. L. (1987), The magnetospheric boundary, in *Physics of Space Plasmas*, edited by T. Chang, G. B. Crew, and J. R. Jasperse, pp. 3–78, Scientific, Cambridge, Mass.
- Siscoe, G. L., G. M. Erickson, B. U. Ö. Sonnerup, N. C. Maynard, K. D. Siebert, D. R. Weimer, and W. W. White (2001), Global role of E_{\parallel} in magnetopause reconnection: An explicit demonstration, *J. Geophys. Res.*, *106*, 13,015.
- Sonnerup, B. U. Ö. (1974), Magnetopause reconnection rate, *J. Geophys. Res.*, *79*(10), 1546–1549.
- Sonnerup, B. U. Ö., and L. J. Cahill (1967), Magnetopause structure and attitude from Explorer 12 observations, *J. Geophys. Res.*, *72*(1), 171–183.
- Stern, D. P. (1973), A study of the electric field in an open magnetospheric model, *J. Geophys. Res.*, *78*(31), 7292–7305.
- Swisdak, M., and J. F. Drake (2007), Orientation of the reconnection X-line, *Geophys. Res. Lett.*, *34*(11), L11106.
- Teh, W.-L., and B. U. Ö. Sonnerup (2008), First results from ideal 2-D MHD reconstruction: magnetopause reconnection event seen by Cluster, *Ann. Geophys.*, *26*(9), 2673–2684.
- Tóth, G., B. van der Holst, I. V. Sokolov, D. L. D. Zeeuw, T. I. Gombosi, F. Fang, W. B. Manchester, X. Meng, D. Najib, K. G. Powell, Q. F. Stout, A. Glocer, Y.-J. Ma, and M. Opher (2012), Adaptive numerical algorithms in space weather modeling, *J. Comp. Phys.*, *231*(3), 870–903.
- Trattner, K. J., J. S. Mulcock, S. M. Petrinc, and S. A. Fuselier (2007), Probing the boundary between antiparallel and component reconnection during southward interplanetary magnetic field conditions, *J. Geophys. Res.*, *112*(A8), A08210.
- Trattner, K. J., S. M. Petrinc, S. A. Fuselier, and T. D. Phan (2012), The location of reconnection at the magnetopause: Testing the maximum magnetic shear model with THEMIS observations, *J. Geophys. Res.*, *117*(A1), A01201.
- Tsyganenko, N. A. (1995), Modeling the Earth’s magnetospheric magnetic field confined within a realistic magnetopause, *J. Geophys. Res.*, *100*(A4), 5599–5612.
- Wilder, F. D., S. Eriksson, K. J. Trattner, P. A. Cassak, S. A. Fuselier, and B. Lybekk (2014), Observation of a retreating X-line and magnetic islands poleward of the cusp during northward interplanetary magnetic field conditions, *J. Geophys. Res.*
- Xiao, C. J., X. G. Wang, Z. Y. Pu, Z. W. Ma, H. Zhao, G. P. Zhou, J. X. Wang, M. G. Kivelson, S. Y. Fu, Z. X. Liu, Q. G. Zong, M. W. Dunlop, K. H. Glassmeier, E. Lucek, H. Rème, I. Dandouras, and C. P. Escoubet (2007), Satellite observations of separator-line geometry of three-dimensional magnetic reconnection, *Nat. Phys.*, *3*, 609.